Mechanism and Machine Theory 74 (2014) 42–57

Contents lists available at ScienceDirect

Mechanism and Machine Theory

journal homepage: www.elsevier.com/locate/mechmt

# Load distribution analysis of clearance-fit spline joints using finite elements

J. Hong, D. Talbot *, A. Kahraman

*Department of Mechanical and Aerospace Engineering, The Ohio State University, 201W. 19th Avenue, Columbus, OH 43210, United States*

ARTICLE INFO

*Article history:*
Received 12 April 2013
received in revised form 4 November 2013
accepted 12 November 2013
Available online xxxx

*Keywords:*
Splines
Load distribution
Finite elements

ABSTRACT

Splines are widely used in mechanical drive systems to transfer rotary motion from an input to an output. Despite their wide application in rotating machinery, very little is known about their contact behavior and load distribution characteristics. In this study, a combined finite element and surface integral contact analysis model is employed in order to investigate load distribution along the spline interfaces. Three loading cases are considered: (i) purely torsional loading representing power transfer through two concentric shafts, (ii) combined torsional and radial loading representing a spur gear–shaft interface, and (iii) combined torsional, radial, and moment loading representing a helical gear–shaft interface. The effect of spline misalignment is investigated along with intentional lead crowning of the contacting surfaces. In addition to spur spline teeth, helical spline teeth are investigated. Influence of intentional mismatch of splines through a slight helix angle applied to the external spline is also investigated within a range of torque transmitted. Finally, the effects of manufacturing tooth indexing error on spline load distributions are quantified using the proposed model.



## 1. Introduction

Splines are widely used in mechanical drive systems to transfer rotary motion and torsion from a shaft to a gear or from a gear to a shaft. The main advantage of splined shafts over keyed shafts is their higher load carrying capacity that often represents better durability performance. Moreover, spline couplings allow for a certain amount of angular misalignment and relative sliding between their internal and external components. They can transfer axial, rotational and torsional load effectively in case of helical gear loading.

The most common failure modes observed in spline joints include surface wear, fretting corrosion fatigue, and tooth breakage. Ku and Valtierra [1] studied wear of misaligned splines experimentally, demonstrating a significant effect of misalignments on the wear of a spline. Brown [2] reported accelerated wear of involute spline couplings in aircraft accessory drives primarily due to spline misalignment and undesirable lubrication conditions.

These experimental studies on splines were instrumental in defining and documenting failure modes in spline interfaces. Yet their contributions to the understanding of spline failure mechanisms were limited without knowing the load distributions along the spline contact interfaces. Review of the literature reveals only a few analytical models on splines, all of which were limited to simple loading conditions due to complexity of the contact in spline interfaces. Volfson [3] proposed a rough estimation of contact force distribution along the axial direction of splines under pure torsion or pure bending loading conditions. Tatur and Vygonnyi [4] developed an analytical model to estimate torque distribution along the face width direction of spline teeth for the case when

* Corresponding author. Tel.: +1 614 688 2930.
*E-mail address:* talbot.11@osu.edu (D. Talbot).

0094-114X/$ – see front matter © 2013 Elsevier Ltd. All rights reserved.
http://dx.doi.org/10.1016/j.mechmachtheory.2013.11.007

the spline joint carries pure torsion. They proposed that the running torque $m(z)$ along the axial direction of the spline be determined by the following differential equation:

$$m(z) = \frac{dT^e(z)}{dz} = c_\varphi\left[\varphi^i(z) - \varphi^e(z)\right] \tag{1}$$

where $T^e(z)$ is the shaft torque, $c_\varphi$ is the torsional stiffness of the spline joint which is assumed to be a constant along the axial direction, and $\varphi^i(z)$ and $\varphi^e(z)$ are twisting angles of the internal spline and external spline respectively. This simplified model requires a user-defined spline torsional stiffness. Barrot et al. [5–7] formulated the spline tooth torsional stiffness in the model of Tatur and Vygonnyi [4] by analyzing spline tooth deflections due to bending, shear, compression and base rotation. They calculated the load distribution along axial direction of splines under pure torsion loading conditions. These analytical models provide an estimate of load distribution along the face width direction of the splines under simple loading conditions, but they fail to predict the load distribution across the spline tooth profile direction. Furthermore, they fall short of handling load distribution of splines under combined loading conditions as is the case for gear–shaft spline joints. Other complicating effects such as spline tooth surface modifications and spline tooth manufacturing errors such as indexing or spacing errors are also not considered in these models.

Another group of more recent studies proposed computational models of splines using the finite element (FE) method or boundary element (BE) method. FE models by Limmer et al. [8], Kahn-Jetter and Wright [9] and Tjernberg [10,11] used commercial FE packages to predict spline load distributions under pure torsion loading, while the last two accounted for effects of certain manufacturing errors as well. FE models for helical spline couplings were proposed by Leen et al. [12–14] and Ding et al. [15–17] for splines under combined torsional and axial loading. Adey et al. [18] developed a model using boundary element method for spline analysis. This model had the capability to analyze combined torsional and bending loading in the presence of certain manufacturing errors. Using Adey's model, Medina and Olver [19,20] studied load distribution of misaligned splines, and the impact of spline pitch errors and lead crown modifications.

The above literature review indicates that there is no widely accepted general analysis tool for spline load distribution. Most of these did not include combined radial, torsional and bending loading conditions experienced by spur and helical gear splines. Under such complex loading conditions, effects of spline tooth modifications and manufacturing errors are not fully understood. Consequences of the common practice of applying an intentional mismatch of splines also remain unknown. Furthermore, extensive parameter studies of the effects of spline tooth modifications and manufacturing errors are also not available. Accordingly, this paper aims at developing FE based computation model of gear–shaft splines. The objectives of this paper are as follows. (i) Develop a computational model of a gear–shaft spline interface under combined torsion, radial forces and tilting moments. (ii) Establish nominal load distribution conditions under pure torsion, spur gear loading (torsion and radial force) and helical gear (torsion, radial force and tilting moment) loading conditions. (iii) Quantify the change to baseline load distributions caused by misalignments, spline tooth (lead and profile) modifications, spline helix angle and intentional helical mismatch. (iv) Investigate the influence of manufacturing errors on baseline spline load distributions.

## 2. Computational model

A commercial FE based contact mechanics model Helical 3D (Advanced Numerical Solutions, Inc.) designed specifically for loaded contact analysis of helical gears is modified here to analyze spline joints. An efficient and accurate finite quasi-prism (FQP) element [21] is used in this model to represent spline surfaces. The core contact solver of this software (CALYX) is based on a formulation by Vijayakar [22], which combines the finite element method and surface integral method to represent the contact bodies, and calculates the load distribution and rigid body displacements by using the linear programming method.

The first phase of contact analysis is to determine the contact zone. CALYX estimates the contact zone by using Hertz's model after locating a set of "primary contact points" on the contacting surfaces and determining relative principal curvatures and directions. The second phase is to compute the compliance matrix and set up the contact equation to be solved by a modified simplex method.

The first step in the process is locating the primary contact point. For this, two contacting surfaces $\Sigma_1$ and $\Sigma_2$ are defined in terms of their curvilinear parameters $s$ and $t$ as $\mathbf{r}_1(s_1,t_1)$ and $\mathbf{r}_2(s_2,t_2)$. The primary contact points are determined and located when $\mathbf{r}_1$ and $\mathbf{r}_2$ become the closest to each other [22]. For this, the surface $\mathbf{r}_1(s_1,t_1)$ is discretized into a grid of points $\mathbf{r}_{1ij}(s_{1i},t_{1j})$. For each of these grid points, a primary contact point $\mathbf{r}_{2ij}(s_{2i},t_{2j})$ is determined such that $\|\mathbf{r}_1(s_1,t_1) - \mathbf{r}_2(s_2,t_2)\|$ is minimum. This extremization is equivalent to solving the following system of nonlinear equations [22]:

$$\begin{cases} \left[\mathbf{r}_{1ij} - \mathbf{r}_2\left(s_{2i}, t_{2j}\right)\right] \cdot \dfrac{\partial \mathbf{r}_2\left(s_{2i}, t_{2j}\right)}{\partial \mathbf{s}_{2i}} = 0 \\ \left[\mathbf{r}_{1ij} - \mathbf{r}_2\left(s_{2i}, t_{2j}\right)\right] \cdot \dfrac{\partial \mathbf{r}_2\left(s_{2i}, t_{2j}\right)}{\partial \mathbf{t}_{2j}} = 0 \end{cases} \tag{2}$$

Newton–Raphson method is used to solve this system of non-linear equations to obtain mating points $\mathbf{r}_{2ij}$ on the second surface for each of the grid points $\mathbf{r}_{1ij}$. Then a refined grid is set up around the point $\mathbf{r}_{1ij}$ such that the separation $\|\mathbf{r}_{1ij} - \mathbf{r}_{2ij}\|$ is the smallest. This process is repeated several times with progressively smaller grids to locate the principal contact point $p$ [22].

The principal curvatures and principal directions of two surfaces at the common contact point $p$ are determined in terms of the coefficients of the first and second fundamental form of the surfaces. For a unit normal vector defined at point $p$ as

$$\mathbf{n} = \frac{\frac{\delta \mathbf{r}}{\delta s} \times \frac{\delta \mathbf{r}}{\delta t}}{\left\| \frac{\delta \mathbf{r}}{\delta s} \times \frac{\delta \mathbf{r}}{\delta t} \right\|}, \tag{3a}$$

the following matrices

$$\mathbf{A} = \begin{bmatrix} \frac{\delta \mathbf{r}}{\delta s} \cdot \frac{\delta \mathbf{r}}{\delta s} & \frac{\delta \mathbf{r}}{\delta s} \cdot \frac{\delta \mathbf{r}}{\delta t} \\ \frac{\delta \mathbf{r}}{\delta t} \cdot \frac{\delta \mathbf{r}}{\delta s} & \frac{\delta \mathbf{r}}{\delta t} \cdot \frac{\delta \mathbf{r}}{\delta t} \end{bmatrix}, \qquad \mathbf{B} = \begin{bmatrix} \mathbf{n} \cdot \frac{\partial^2 \mathbf{r}}{\partial s^2} & \mathbf{n} \cdot \frac{\partial^2 \mathbf{r}}{\partial s \partial t} \\ \mathbf{n} \cdot \frac{\partial^2 \mathbf{r}}{\partial t \partial s} & \mathbf{n} \cdot \frac{\partial^2 \mathbf{r}}{\partial t^2} \end{bmatrix} \tag{3b, c}$$

contain the coefficients of the first and second fundamental form of the surface, respectively. The corresponding eigenvalue problem

$$\mathbf{B}\boldsymbol{\lambda} = \kappa \mathbf{A}\boldsymbol{\lambda} \tag{3d}$$

yields eigenvalues $\kappa^{(1)}$ and $\kappa^{(2)}$ that are the principal normal curvatures and the corresponding eigenvectors $\boldsymbol{\lambda}_1$ and $\boldsymbol{\lambda}_2$. With the eigenvectors normalized (i.e. $\boldsymbol{\lambda}_m^T \mathbf{A}\, \boldsymbol{\lambda}_m = 1\ m = 1, 2$), the two unit vectors in the principal directions corresponding to the principal curvatures are found as [22]:

$$\begin{cases} \mathbf{t}^{(1)} = \boldsymbol{\lambda}_1^T \begin{Bmatrix} \partial \mathbf{r}/\partial s \\ \partial \mathbf{r}/\partial t \end{Bmatrix} \\ \mathbf{t}^{(2)} = \boldsymbol{\lambda}_2^T \begin{Bmatrix} \partial \mathbf{r}/\partial s \\ \partial \mathbf{r}/\partial t \end{Bmatrix} \end{cases} \tag{4}$$

With the principal curvatures $\kappa_n^{(1)}$ and $\kappa_n^{(2)}$ and the principal directions $\mathbf{t}_n^{(1)}$ and $\mathbf{t}_n^{(2)}$ of surface $\Sigma_n$ $(n = 1, 2)$ defined at $p$, the unit vectors in the directions of these principal relative curvatures are given as:

$$\begin{cases} \boldsymbol{\tau}^{(1)} = \mathbf{t}_1^{(1)} \cos\Phi + \mathbf{t}_1^{(2)} \sin\Phi \\ \boldsymbol{\tau}^{(2)} = -\mathbf{t}_1^{(1)} \sin\Phi + \mathbf{t}_1^{(2)} \cos\Phi \end{cases} \tag{5a}$$

where the angle $\theta$ between $\mathbf{t}_2^{(1)}$ and $\mathbf{t}_1^{(1)}$, and the angle $\Phi$ between $\boldsymbol{\tau}^{(1)}$ and $\mathbf{t}_1^{(1)}$ are defined as [22]:

$$\begin{cases} \theta = \tan^{-1}\left( \dfrac{\mathbf{t}_2^{(1)} \cdot \mathbf{t}_1^{(2)}}{\mathbf{t}_2^{(1)} \cdot \mathbf{t}_1^{(1)}} \right) \\ \Phi = \dfrac{1}{2} \tan^{-1}\left[ \dfrac{\left(\kappa_2^{(1)} - \kappa_2^{(2)}\right) \sin(2\theta)}{\left(\kappa_1^{(1)} - \kappa_1^{(2)}\right) + \left(\kappa_2^{(1)} - \kappa_2^{(2)}\right) \cos(2\theta)} \right] \end{cases} \tag{5b}$$

Once the primary contact points are located and the relative curvatures are obtained, Hertzian theory is used to predict the size of the contact zone and consequently a grid of points in the contact zone is laid out on both surfaces. Then a surface integral method near the contact zone and a finite element method away from the contact zone are combined to predict cross compliance terms between the set of grid points.

The displacement $u(\mathbf{r}_{ij};\mathbf{r})$ at a field point $\mathbf{r}$ caused by a unit normal force at surface grid point $\mathbf{r}_{ij}$ is given as [22]:

$$u\left(\mathbf{r}_{ij};\mathbf{r}\right) = \left(u^{(\mathrm{si})}\left(\mathbf{r}_{ij};\mathbf{r}\right) - u^{(\mathrm{si})}\left(\mathbf{r}_{ij};\mathbf{q}\right)\right) + u^{(\mathrm{fe})}\left(\mathbf{r}_{ij};\mathbf{q}\right). \tag{6}$$

Here $\mathbf{q}$ is some location inside the body on a matching surface, sufficiently far beneath the tooth surface. The first two terms in this equation denote the relative deflection of $\mathbf{r}$ with respect to $\mathbf{q}$, which is evaluated using the surface integral formulae. The third term denotes the displacement of $\mathbf{q}$, which is computed using finite element method [23]. The point $\mathbf{q}$ is chosen such that elastic half space assumption will be valid and the finite element prediction will not be significantly affected by local stresses on the surface. The surface integral and finite element solutions are combined along this matching surface interface, as described in detail in Ref. [22]. The combination of surface integral formulae and finite element method described above provides an accurate and numerically efficient way of obtaining the compliance matrix for the contacting bodies. Contact equations are set up using the compliance matrix and solved by a modified Simplex algorithm of linear programming, which is described in detail in Ref. [24].

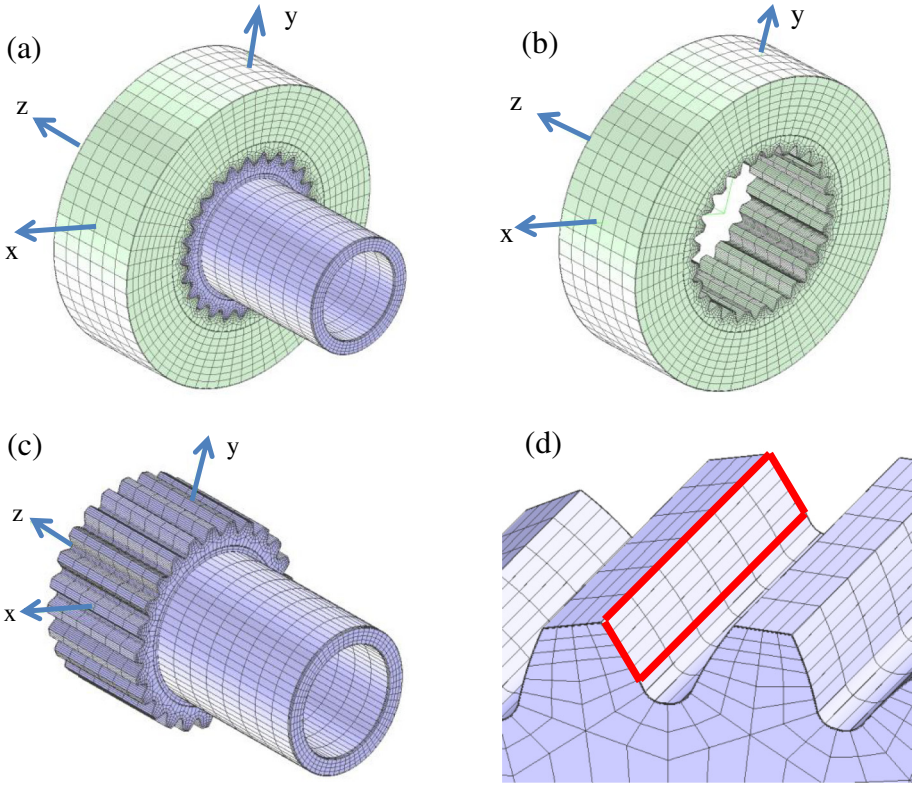


**Fig. 1.** Spline finite element model; (a) spline interface, (b) internal spline, (c) external spline and shaft, (d) potential contact area and contact elements.

## 3. Finite element model of an example spline and analysis results

Fig. 1 shows the finite element model for an example spline joint that is designed according to ANSI B92.1-1996 standard [25]. The parameters of this clearance-fit spline are listed in Table 1.

The system model consists of a shaft, an external spline and an internal spline. Over the potential contact area, the model shown in Fig. 1 uses a contact grid with $M$ number of elements in the face width direction and $N$ number of elements along the profile direction. Within each contact element the user can define the number of contact grids along face width and profile direction as Helical 3D employs a hierarchy of substructures and sub-substructures to generate the spline model. With this, the program inverts stiffness matrices of smaller sizes before substituting them into the global matrix. In this study, 2 contact grids are defined in both face width direction and profile direction within each contact element. Width of the contact cells is defined such that $2N$ grids in the profile direction can capture all the potential contact on the tooth. With this, a spline joint with $Z$ teeth would have a total of $Z \times 2M \times 2N$ grid cells defining the contacts along the drive flanks of the teeth. In the model of Fig. 1(d),

**Table 1**
Parameters of an example spline design used in this study.

| | External spline | Internal spline |
|---|---|---|
| Number of teeth | 25 | |
| Spline module [mm] | 3.175 | |
| Pressure angle | 30° | |
| Base diameter [mm] | 68.732 | |
| Face Width [mm] | 50 | |
| Major diameter [mm] | 82.550 | 85.725 |
| Form diameter [mm] | 76.022 | 82.728 |
| Minor diameter [mm] | 73.025 | 76.200 |
| Circular space width [mm] | – | 5.055 |
| Circular tooth thickness [mm] | 4.981 | – |
| Inner rim diameter [mm] | 58 | 95 |
| Outer rim diameter [mm] | 64 | 150 |
| Inner shaft diameter [mm] | 45 | – |
| Outer shaft diameter [mm] | 58 | – |
| Profile crown [μm] | 2.5 | 0.0 |

$M = 6$ and $N = 5$ was deemed to provide a reasonable load distribution resolution while keeping the computational time relatively short (a single position load distribution analysis of the spline joint of Fig. 1 required 40 min. on a PC with a 3.39 GHz processor). The model allows intentional deviations from the involute spline tooth surfaces such as profile and lead modifications as in spur and helical gears to prevent any undesirable edge contact conditions. In addition, a similar contact grid with the same resolution can be defined along the other $Z$ tooth surfaces forming the coast side to capture any back side contacts.

This example spline interface is loaded in three different ways. In the first case, a moment (torsion) $T$ is applied to the end of the shaft as shown in Fig. 2(a) while the cylindrical disk having the internal spline is constrained along its perimeter to represent a purely torsional loading of the spline with no radial force and tilting moment. The second loading case shown in Fig. 2(b) represents a spline supporting a spur gear where $T$, applied torque, is balanced by the mesh force $F_n = 2T/(d_p \cos \alpha_n)$ where $\alpha_n$ and $d_p$ are the normal pressure angle and pitch circle diameter of the spur gear, respectively, and $F_n$ acts on the transverse plane of the gear along the line of action, in the process applying a torque $T$ and radial force $F = F_n$ to the spline interface. In the model of Fig. 2(b), a spur gear tooth is defined as shown and $F$ is applied to it at the tooth center along the line of action. The translational and rotational motions along the $x$ and $y$ directions of the external spline shaft are constrained. The third loading condition considered in this study represents the case of a spline supporting a helical gear as shown in Fig. 2(c). In this case, the gear mesh force $F_n$ on the plane of action in the normal direction has a tangent component $F_t = 2T/d_p$, a radial component $F_r = F_t \tan \alpha_n/\cos \beta$ and an axial component $F_a = F_t \tan \beta$, where $\alpha_n$, $\beta$ and $d_p$ are the normal pressure angle, helix angle and pitch circle diameter of the gear, respectively. This results in a torsion $T$ about the rotational axis $z$ of the shaft, radial forces $F_x = F_t, F_y = -F_r$, and tilting moment $M_x = T \tan \beta$ about the $x$ axis in Fig. 2(c). In this case, the moment $M_x$ was applied in addition to $F_x$ and $F_y$ to the gear tooth and $T$ applied to the input end of the shaft.

### 3.1. Influence of loading conditions

#### 3.1.1. Pure torsion loading case

In case of pure torsion loading of Fig. 2(a), one would expect identical load distributions on each spline tooth with load varying along face width and profile directions. Fig. 3(a) shows various views of the shaft spline to demonstrate the loads carried by individual contact grid cells on each tooth. As this type of a representation of the tooth load distributions is not practical, the contact surface of each tooth of the shaft spline was mapped to a rectangular window as shown in Fig. 3(b) with the load distribution of the tooth surface displayed on this window. Using this method, load distributions on all of the teeth can be viewed simultaneously and conveniently as shown in Fig. 4 for this torsional loading case.

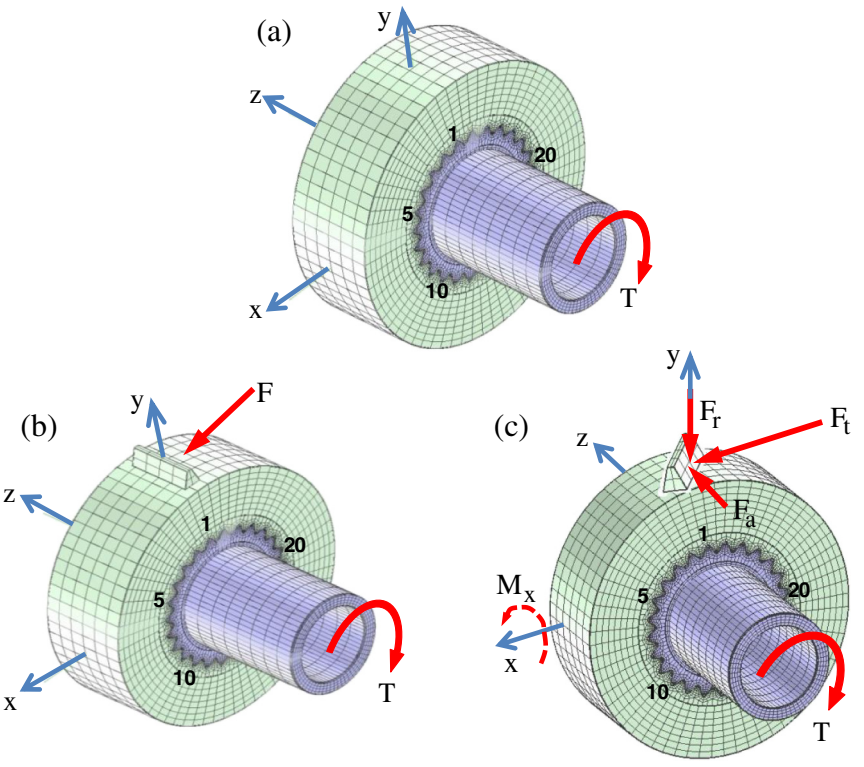


**Fig. 2.** A spline model with different loading conditions; (a) pure torsion loading, (b) spur gear loading, and (c) helical gear loading.

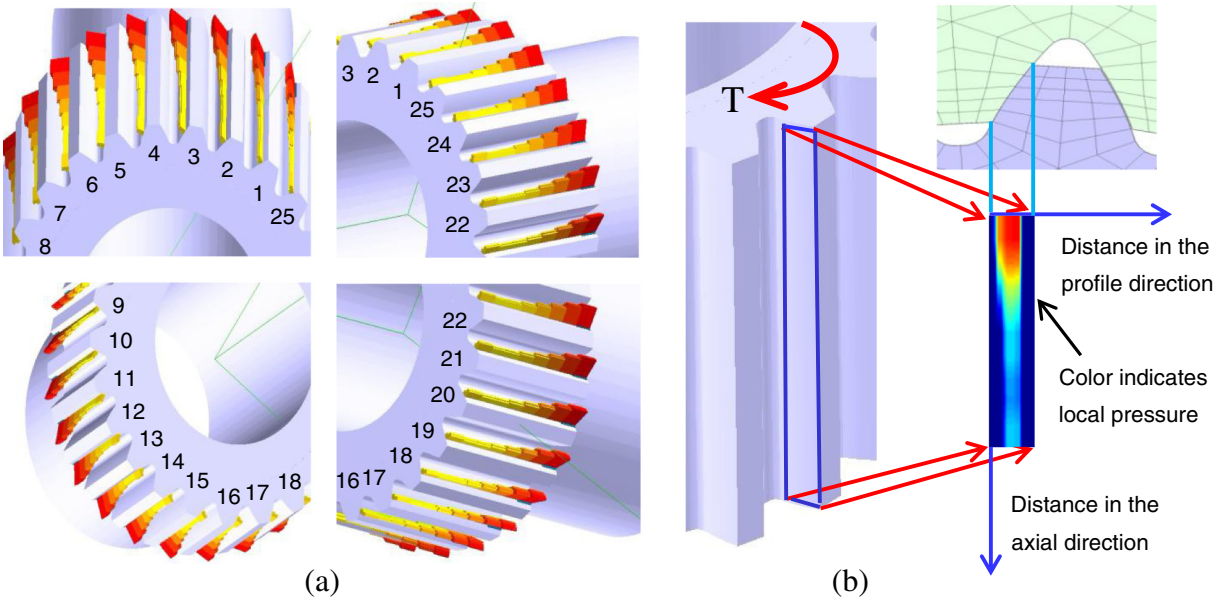


**Fig. 3.** (a) Load distribution of a spline under pure torsion loading, and (b) mapping of the load distribution on a tooth to a rectangular window.

Fig. 4 shows the load distributions on the spline teeth under pure torsion at torque levels of $T = 550$, 1100, 1650 and 2200 Nm. At $T = 550$ Nm, maximum contact stress is predicted to be about 36 MPa that occurs at the edge on the input side where the torque is applied to the shaft. The contact stresses reduce significantly with the axial distance from this edge. Non-uniform load distributions become clearer with increased $T$ while the location of maximum stress remains at the input-side edge. The maximum contact stresses are 52, 60 and 69 MPa at this locality for $T = 1100$, 1650 and 2200 Nm, respectively. Meanwhile, the maximum contact stresses along the mid-plane of the spline joint are only 20, 28, 30 and 31 MPa for $T = 550$, 1100, 1650 and 2200 Nm, respectively. It is noted that as the torque increases, the contact area gradually extends towards the edge of the spline teeth along the profile direction and the contact stress increases simultaneously, with the load distribution pattern remaining the same.

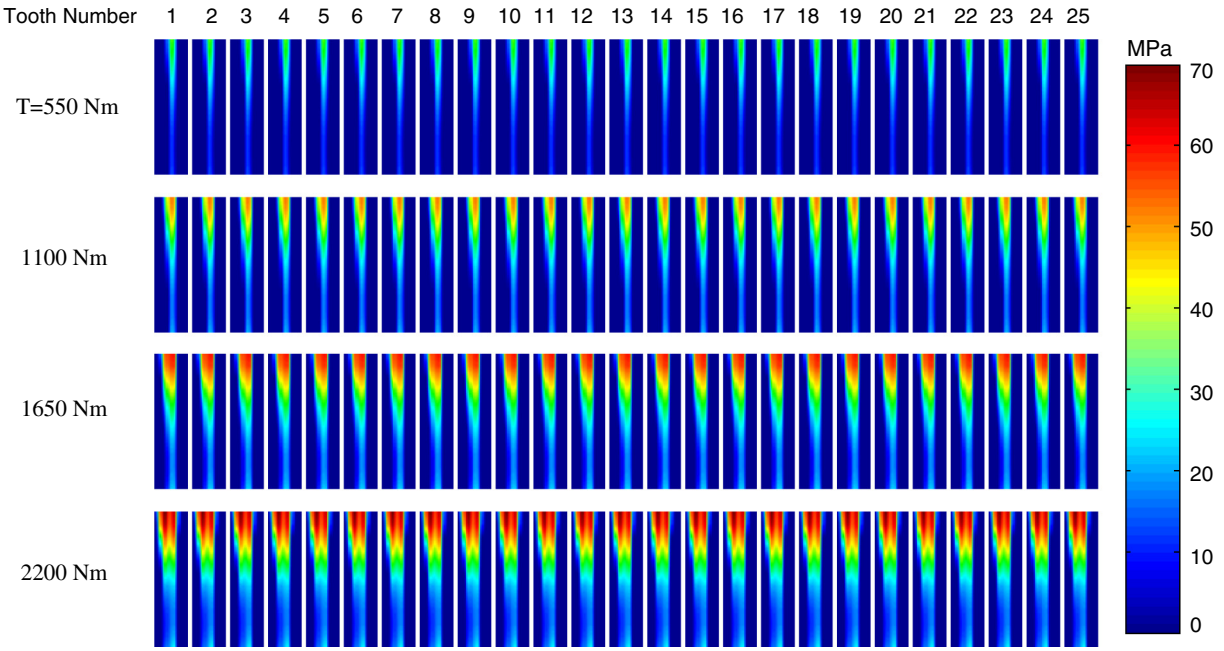


**Fig. 4.** Load distributions of the example spline under pure torsion loading at different torque levels.

*3.1.2. Spur gear loading case*

In a spur gear loading condition, splines are subject to combined torsion and radial load. This asymmetrical loading leads to different load distributions on different spline teeth. Fig. 5 shows the resultant load distributions for the same torque values of $T = 550$, 1100, 1650 and 2200 Nm. Here, relevant spur gear tooth parameters are the normal pressure angle of $\alpha_n = 20^\circ$, and the pitch circle diameter of $d_p = 160$ mm. Two main observations can be made from this figure. First of all, load sharing along the face width direction is still biased towards the side where torque applied. Secondly, load distributions are no longer identical for all spline teeth since the loading is no longer axisymmetric. With tooth #1 centered below (and closest to) the gear mesh, teeth #1–8 and #21–25 are shown to experience larger loads while teeth #9–#20 bear less load. For instance, the resultant maximum contact stresses at $T = 2200$ Nm are 73, 61, 60 and 92 MPa for teeth #5, #10, #15 and #24, respectively, as a direct consequence of this unequal loading. The resultant total spline tooth forces are shown in Fig. 6 for the same loading conditions at different torque levels. With the nominal spline tooth force defined as $\overline{F}_{st} = T/(ZR_b)$ where $R_b$ is the base radius of the spline joint and $Z$ is the number of teeth, the ratio of actual tooth force to nominal tooth force $F_{st}/\overline{F}_{st}$ are 1.55, 0.49, 0.23 and 2.47 for the same teeth #5, #15, #20 and #24, respectively, at $T = 2200$ Nm. This indicates that some teeth carry more than twice their nominal (torsion only) share.

*3.1.3. Helical gear loading case*

As stated earlier and shown graphically in Fig. 2(c), helical gear loading applies a combination of torsion, $T$, tangential force, $F_t$, radial force, $F_r$ and tilting moment, $M_x$. Fig. 7 shows the resultant load distributions on different teeth of the spline under helical gear loading for the same torque values of $T = 550$, 1100, 1650 and 2200 Nm with a gear helix angle $\beta = 15^\circ$ and transverse tooth geometry remaining the same as the spur gear above. In comparison to Fig. 5 for spur gear loading, helical gear loading maintains the same qualitative load sharing characteristics of spline teeth. It shows that teeth #1–8 and #21–25 carry larger load, while teeth #9–20 are loaded less. This can be explained by the fact that the spline interface transmitted the same radial load in spur gear loading and helical gear loading conditions. However, a remarkable difference is observed that axial load distribution on teeth #19–25 and #1–2 is biased to the opposite side to which torque is applied. This is due to the additional tilting moment $M_x$ transmitted over the spline interface, which causes the load on some teeth to be biased to the other side to balance it. Fig. 7 also shows that an increase of torque would only extend the area of contact and increase the contact stress, not affecting the load distribution patterns significantly.

Fig. 8 shows the load distributions on the spline teeth at $T = 2200$ Nm for different gear helix angles of $\beta = 10^\circ$, $15^\circ$, $20^\circ$, and $25^\circ$. Transverse geometry parameters of these helical gears are the same as the spur gear above. It is observed that as $\beta$ increases, the load on each tooth gets more concentrated on the side where the load is biased. For instance, loads on teeth #3–10 are concentrated to the side where the torque is applied, while loads on teeth #20–25 are concentrated to the opposite side. The maximum contact stresses are 109, 129, 212, and 463 MPa for gear helix angle $\beta = 10^\circ$, $15^\circ$, $20^\circ$ and $25^\circ$, respectively. The corresponding tilting moments are $M_x = 388$, 589, 801, 1026 Nm, respectively. The load concentration increases significantly because of the larger resultant tilting moment on the spline when the gear helix angle increases.

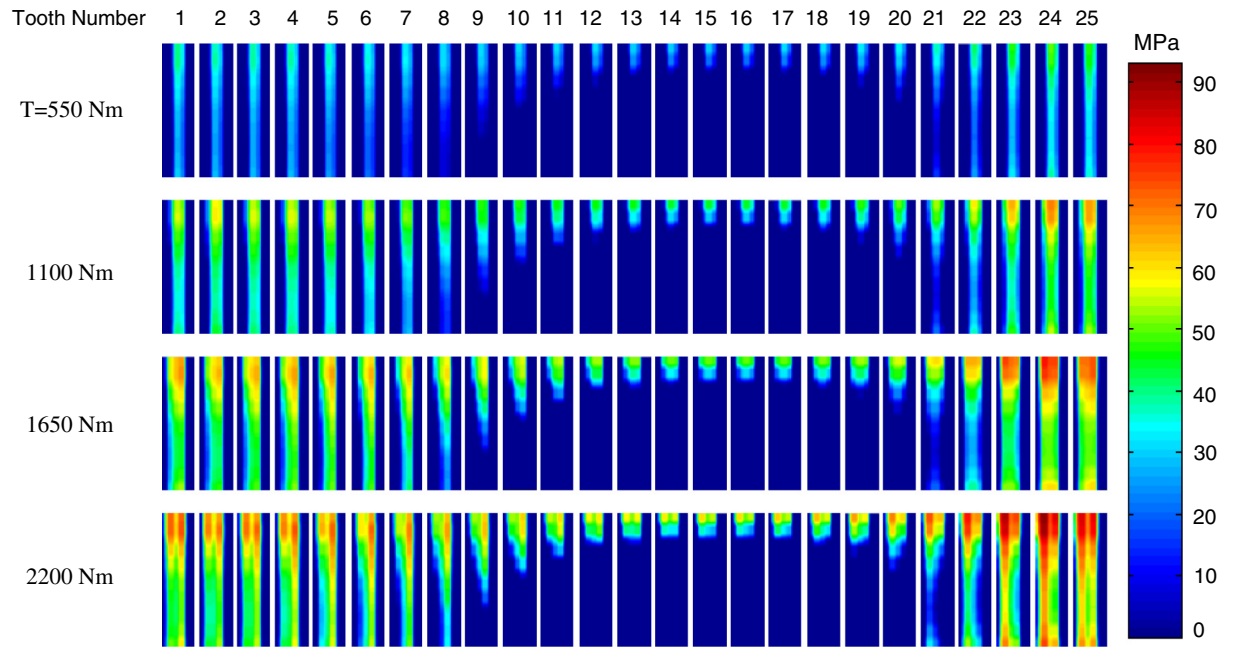


**Fig. 5.** Load distributions of a spline under spur gear loading at different torque levels.

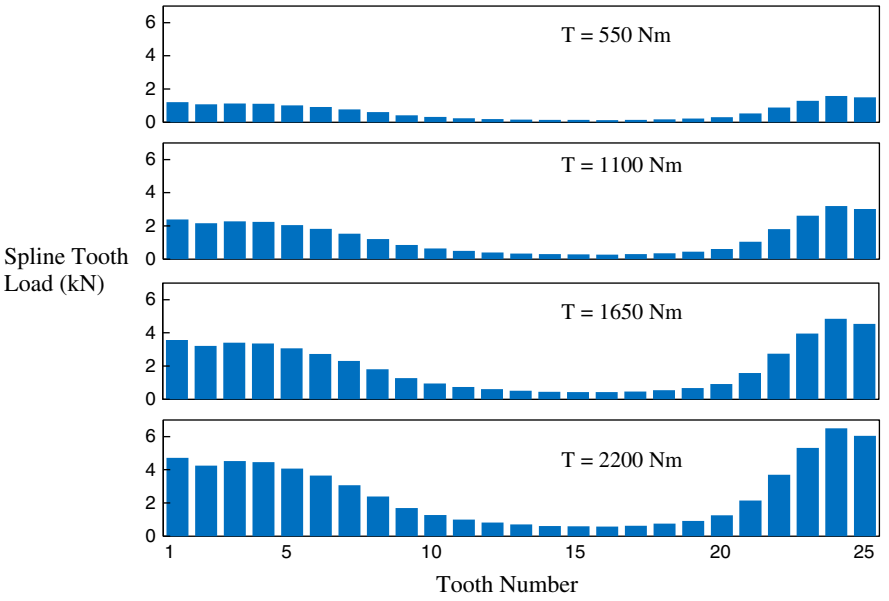


**Fig. 6.** Tooth loads of a spline under spur gear loading at different torque levels.

### 3.2. Effect of design variations to the nominal system

#### 3.2.1. Misalignment and lead crown modifications

Misalignment of spline couplings has been recognized as harmful to splines because it causes significant load concentration on spline teeth, and accelerates wear and fretting fatigue of splines [2,20]. Fig. 9 shows the load distributions on the spline with different misalignments $\varphi = 0^{\circ}, 0.04^{\circ}, 0.08^{\circ}$ and $0.12^{\circ}$ at a torque level of 2200 Nm. It is observed here that the load distribution is biased similar to that of the helical gear loading because the tilting moment caused by misalignment has a dominant effect on the load distribution. It is also noted that the increase of misalignment leads to a significantly larger load concentration at the end of the spline in the axial direction, due to larger tilting moment resulting from increased misalignment.

Significant load concentration was observed in both misaligned splines and splines experiencing helical gear loading. A lead crown modification along the face-width of the spline can be expected to relieve some this load concentration. Fig. 10 shows load

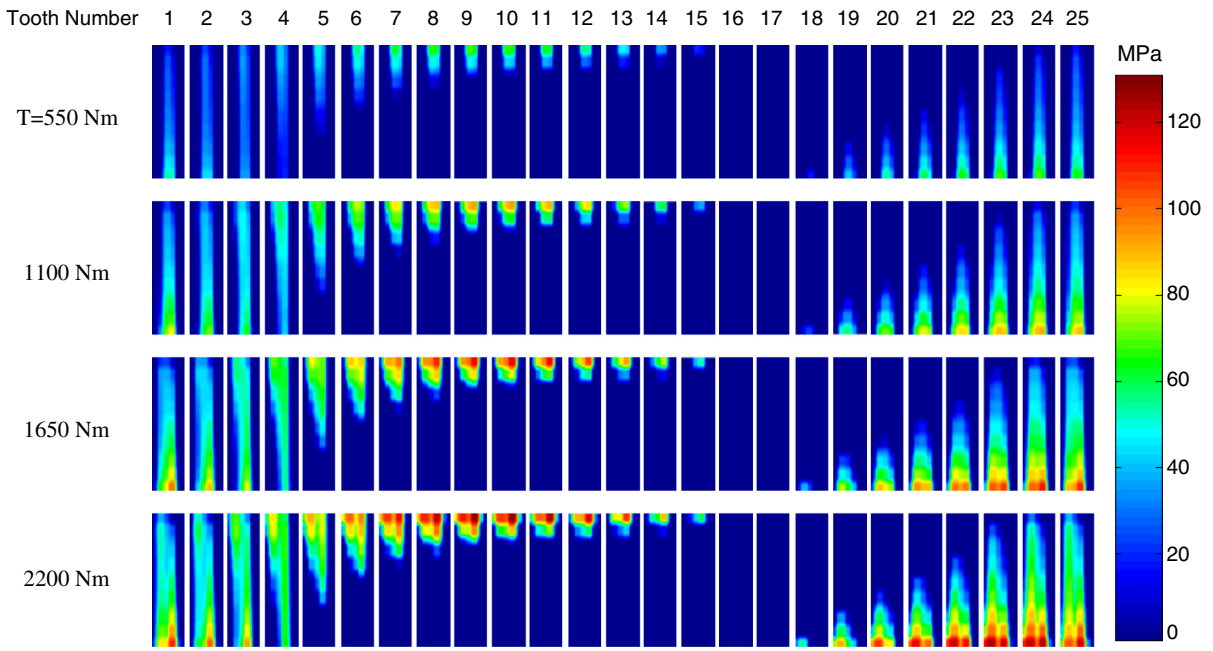


**Fig. 7.** Load distributions of a spline under helical gear loading at different torque levels, gear helix angle, $\beta = 15^{\circ}$.

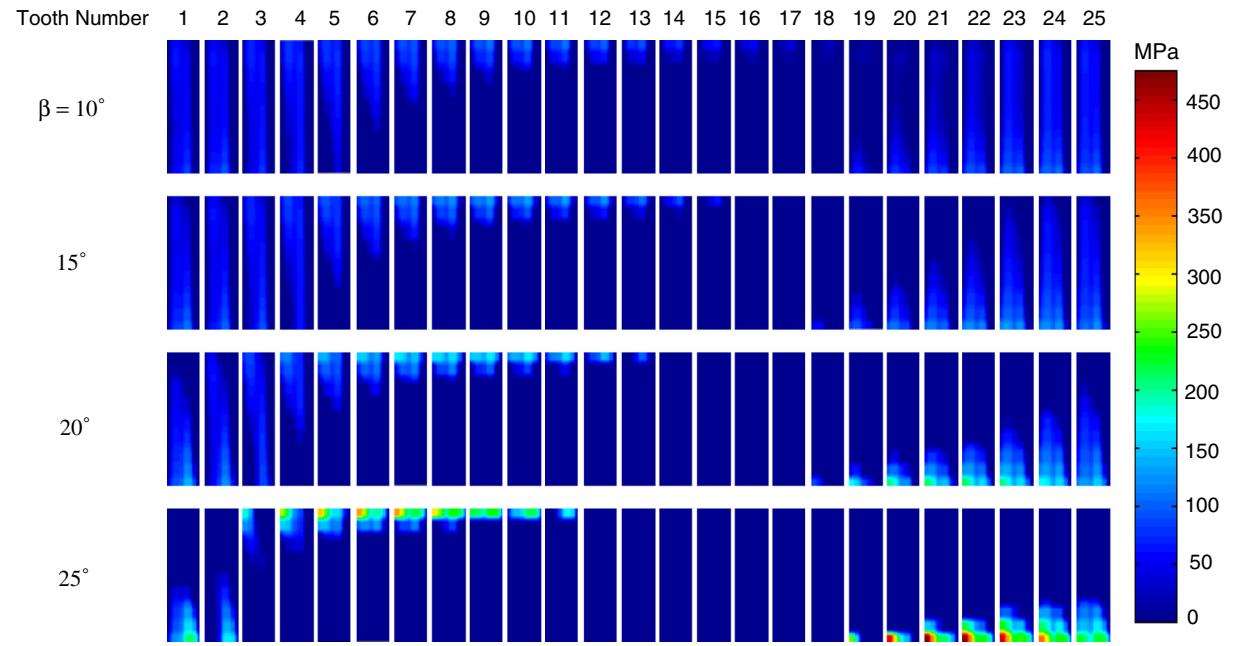


**Fig. 8.** Load distributions of a spline under helical gear loading with different helix angles, $\beta$, at $T = 2200$ Nm.

distributions of a spline having a misalignment of $\varphi = 0.12^{\circ}$ along with different lead crown modification magnitudes of $\delta = 0$, 20, 40 and 60 μm at $T = 2200$ Nm under pure torsion loading. It is observed that the crown modification moves the load from the edge to the center of the spline, in the process reducing the maximum contact stresses significantly. The maximum contact stresses are 261, 166, 158, 166 MPa, respectively, for lead crown magnitudes $\delta = 0$, 20, 40, 60 μm indicating that the optimum lead crown magnitude is 40 μm in this case. It is also noted that when the lead crown modification is increased to 60 μm, only a small portion of the spline tooth face width carries the load. This indicates that a moderate lead crown modification can reduce load concentration effectively while maintaining the spline's load carrying capacity, while excessive amounts of lead crown modifications would increase contact stress and reduce the load bearing capacity of the spline.

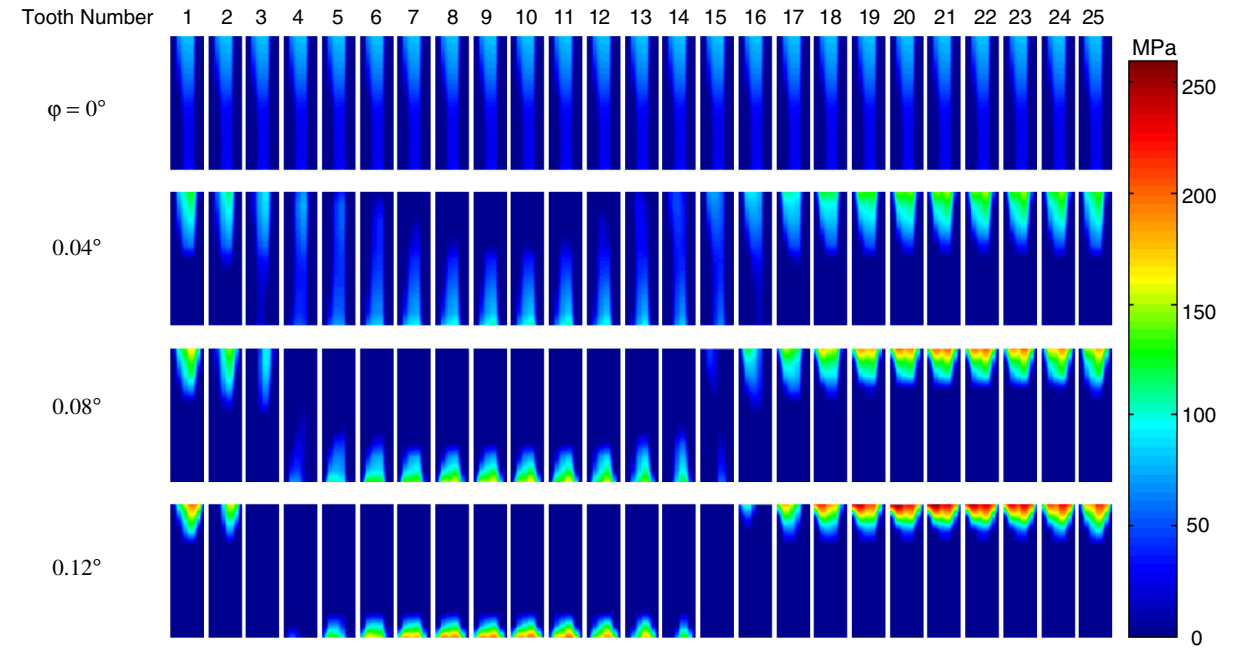


**Fig. 9.** Load distributions of a misaligned spline having different misalignment angles, $\varphi$, at $T =$ Nm.

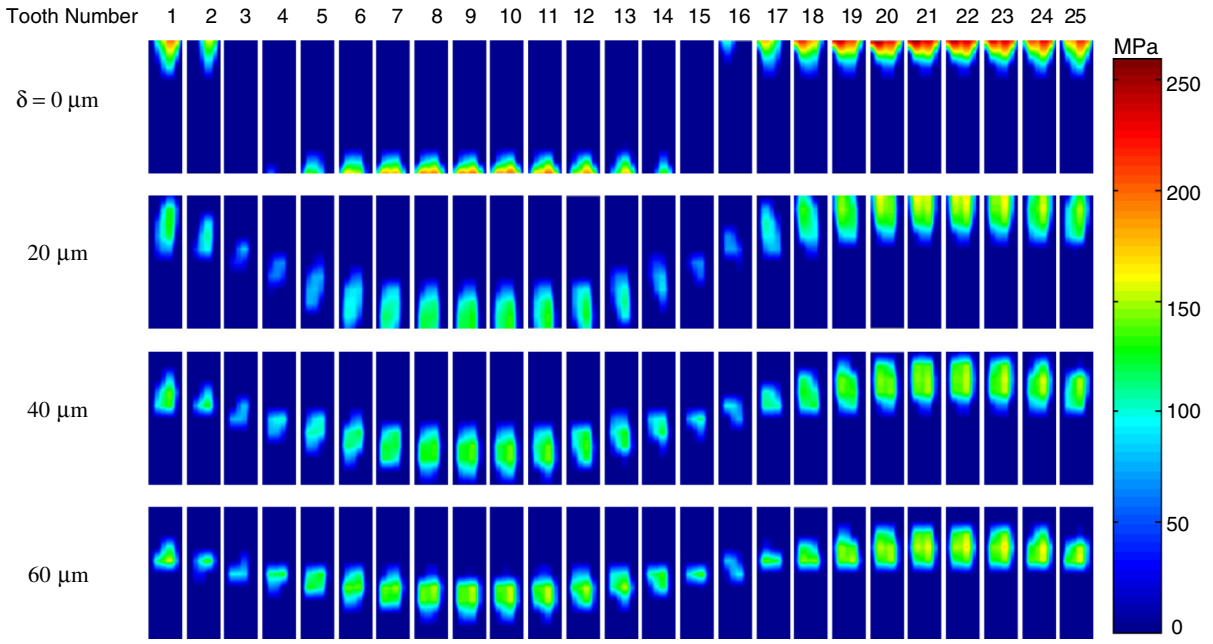


**Fig. 10.** Load distributions of a misaligned spline having different lead crown modification magnitudes, $\delta$, at $T = 2200$ Nm and $\varphi = 0.12°$.

Fig. 11 shows load distributions on the splines with different lead crown modification magnitudes of $\delta = 0, 20, 40$ and 60 μm for helical gear loading with $\beta = 20°$ at $T = 2200$ Nm. The maximum contact stresses are 212, 209, 244 and 315 MPa for lead crown magnitudes $\delta = 0, 20, 40$ and 60 μm, respectively. Unlike in the misaligned spline case, lead crown modification under a helical gear loading condition neither reduces load concentration, nor moves the tooth load from the edge to the center. This occurs because the moment acting on the spline remains a constant for a given torque in helical gear loading despite the lead crown modification. The biased load concentration exists no matter how much lead crown modification is adopted. Meanwhile, in misaligned splines, lead crown modification effectively reduces the tilting moment acting on the spline thus reducing load concentration and improving the load distribution of the spline.

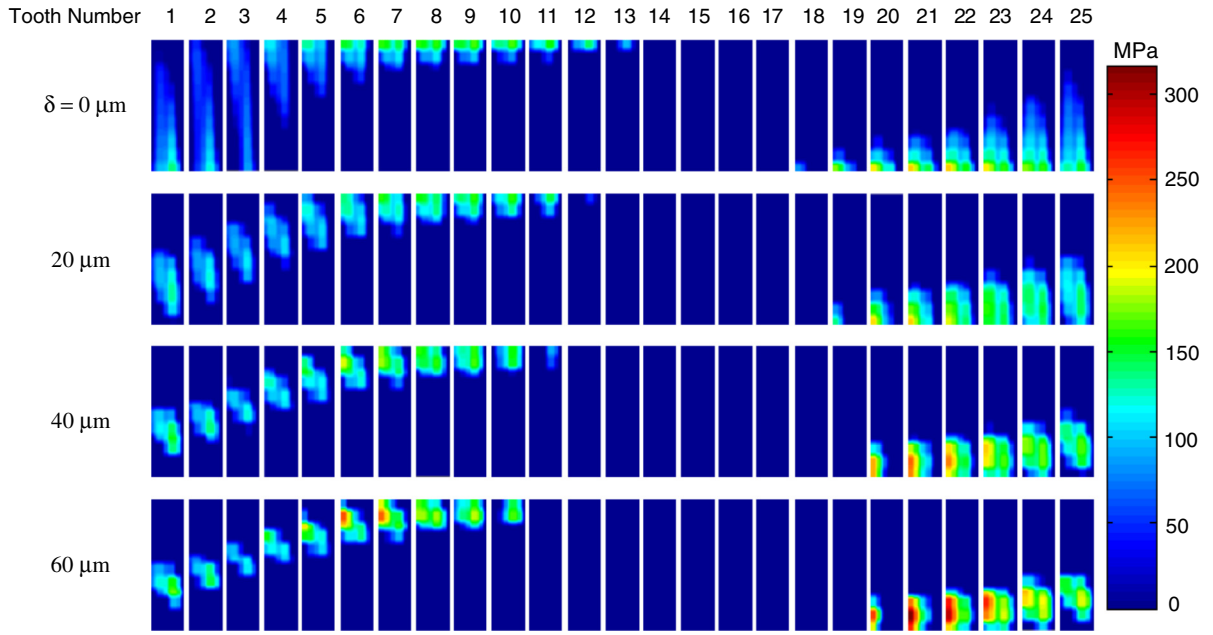


**Fig. 11.** Load distributions of a spline under helical gear loading having different lead crown modification magnitudes, $\delta$, at $T = 2200$ Nm, and $\beta = 20°$.

*3.2.2. Helical splines*

Fig. 12 shows the load distributions of helical splines having different helix angles of $\gamma = -20^{\circ}, -10^{\circ}, 0^{\circ}, 10^{\circ}$ and $20^{\circ}$ under helical gear loading condition with a right-hand helical gear ($\beta = 20^{\circ}$) as shown in Fig. 2(c) at $T = 2200$ Nm. A negative spline helix angle represents a left-handed helix and a positive helix angle represents a right-handed helix. It is observed that a right-hand spline helix helps reduce load concentration, and a left-hand spline helix condenses the load concentration. For instance, the maximum contact stresses are 212 MPa for a spur spline ($\gamma = 0^{\circ}$) under helical gear loading with a right-hand helical gear. The maximum contact stress increases dramatically to 448 and 1081 MPa for left-hand spline helix angles of $\gamma = -10^{\circ}$ and $-20^{\circ}$, respectively. On the other hand, the maximum contact stresses drop significantly to 127 and 103 MPa for right-handed splines with helix angles $\gamma = 10^{\circ}$, and $20^{\circ}$, respectively. The maximum contact stress is reduced by more than 50% and more teeth are observed to carry load as shown in Fig. 12. The dominant factor is that the spline helix introduces an axial load, which can either increase the tilting moment or counterbalance the tilting moment depending on its direction. For a spline loaded by a right-handed gear, a right-hand spline helix would induce an axial load to counterbalance the tilting moment thus reducing the load concentration. On the other hand, a left-hand spline helix would induce an axial load, which would increase the tilting moment thus resulting in larger load concentration on the spline teeth. The result implies that in helical gear loading conditions, selecting a helical spline with the same helix direction as that of the helical gear could reduce the load concentration, and improve load distribution.

*3.2.3. Intentional lead mismatch*

Intentional lead mismatch of splines, introducing a slight helix angle to the external spline and none to the internal spline, is used in high-torque applications. As this mismatch is much larger than what can be accommodated by the circumferential clearance, it introduces a torsional wind-up as a preset. Fig. 13(a) shows the pitch circle plot of mismatched splines, from which it is clearly seen the external spline and the internal spline are in contact when unloaded. Fig. 13(b) shows the load distribution matrix of intentionally mismatched splines with different mismatch values of $\lambda = 0$, 5, 10, 15, 20 and 25 μm at various torque levels of $T = 0$, 1100, 2200, 3300 and 4400 Nm under pure torsion loading. As shown before, load distribution is identical on every tooth under pure torsional loading. Moreover, backside contact occurs in intentionally mismatched splines. Therefore, load distribution on the driving side (A) and the back side (B) of a single spline tooth is selected to represent the whole spline.

It is observed that at low torque levels, contact occurs on both the driving and back sides, and contact stress increases as intentional mismatch value increases. For instance, the maximum contact stresses under zero torque load are 0, 44, 70, 91, 109, 122 MPa for mismatch values $\lambda = 0$, 5, 10, 15, 20 and 25 μm, respectively. It is also noted that at high torque levels, the backside contact vanishes and load concentration on the driving side moves from one side to the other as magnitudes of mismatch increase. For a given torque level, there is an optimum amount of mismatch, which helps distribute the load evenly along spline tooth such as the case of $\lambda = 10$ μm at $T = 3300$ Nm shown in Fig. 13(b). Fig. 14 is a plot of maximum contact stress versus the

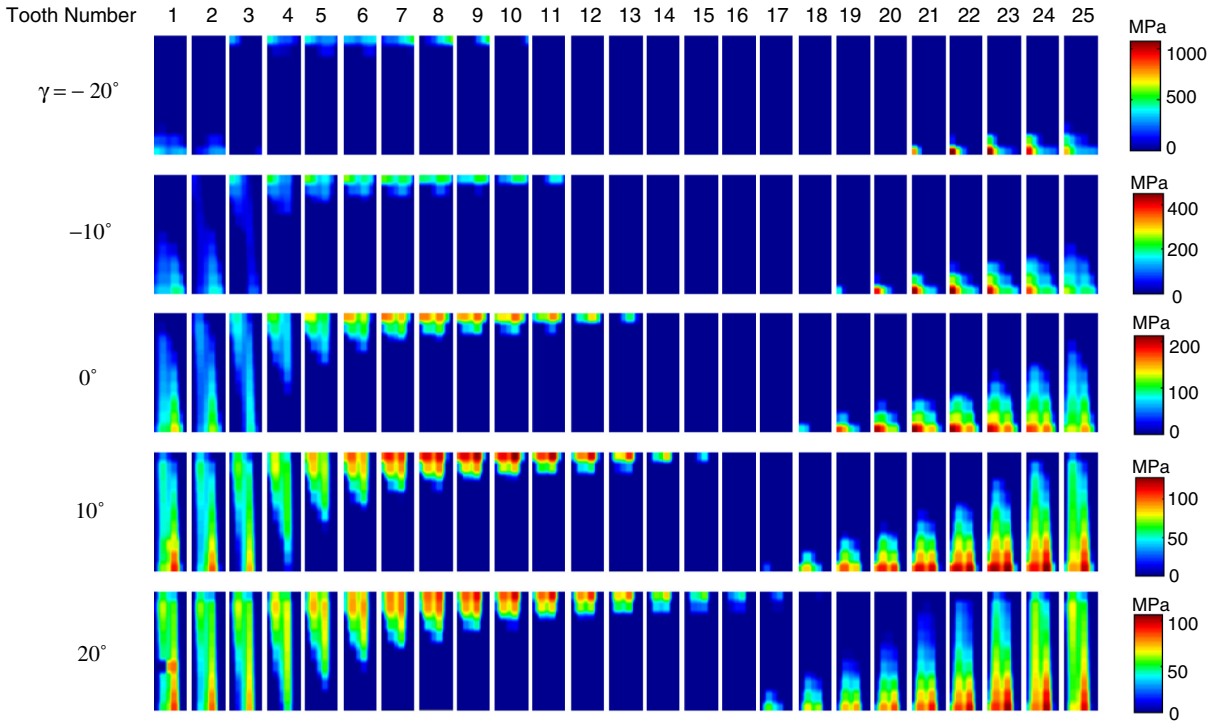


**Fig. 12.** Load distributions of helical splines having different spline helix angles, γ, under helical gear loading with a gear helix angle, $\beta = 20^{\circ}$, at $T = 2200$ Nm.

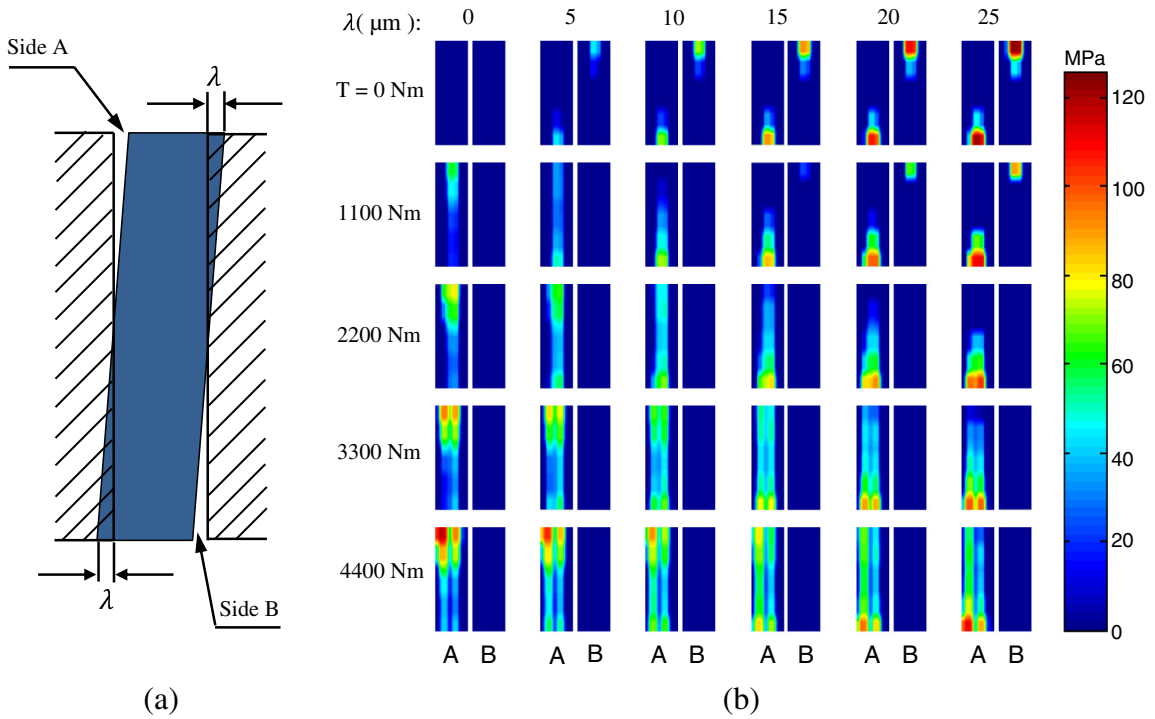


**Fig. 13.** (a) Intentional mismatch, λ, of a spline tooth on the pitch circle; (b) Load distributions of an intentionally mismatched spline having various mismatch magnitudes, λ, at different torque levels.

amount of spline mismatch at different torque levels. The results illustrate that there is an optimum mismatch for a given design torque that reduces the maximum contact stress by providing an evenly distributed spline load.

### 3.3. Effect of spline tooth indexing errors

Investigations of spline load distributions discussed above all assumed perfect tooth geometry, ignoring the effect of tooth indexing errors. However, it occurs frequently that some spline teeth exhibit heavier damage than others, which might be caused by spline tooth indexing errors [20,26]. In order to demonstrate the effect of indexing errors on spline load distributions, a positive indexing error of $\xi_{13} = 5$ μm is applied to tooth #13 of the example spline defined in Table 1. Fig. 15 shows the load distributions on the spline teeth under pure torsion loading conditions at $T = 550$, 1100, 1650 and 2200 Nm. In comparison to Fig. 4 for the pure torsion loaded spline with perfect geometry, this indexing error on tooth #13 results in load concentration on

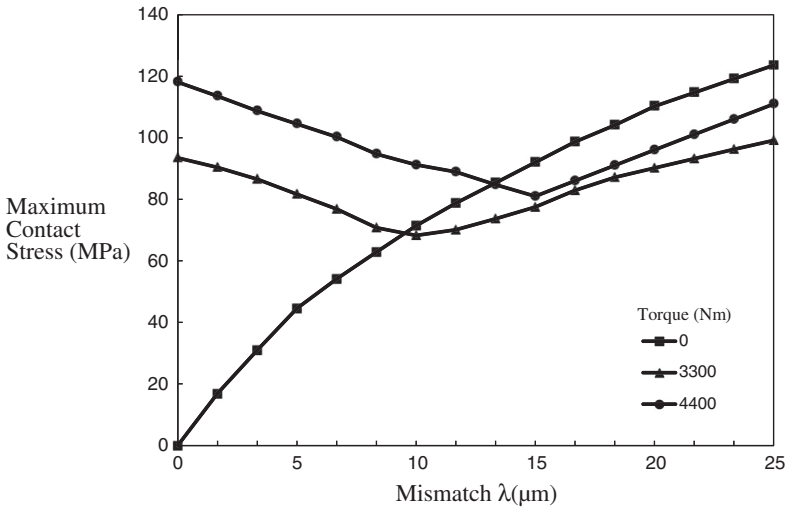


**Fig. 14.** Maximum contact stress versus mismatch magnitude, λ, at different torque levels.

tooth #13, with little or no load on teeth adjacent to tooth #13. For example, at $T = 2200$ Nm, the maximum contact stress is 69 MPa when there is no indexing error, which is almost doubled to 118 MPa when an indexing error of 5 μm exists. Fig. 16 shows the loads carried by each tooth of the spline. Again, denoting the nominal tooth force as $\overline{F}_{st} = T/(ZR_b)$, then the ratios of actual tooth force to nominal tooth force on tooth #13 are 9.3, 7.1, 5.9, 5.2 for $T = 550$, 1100, 1650 and 2200 Nm, respectively.

A spline joint with a random tooth indexing error distribution is considered next. Fig. 17 shows the randomly generated tooth indexing error sequence considered together with the corresponding spline load distributions at $T = 550$, 1100, 1650 and 2200 Nm. Load concentrations, similar to that in Fig. 15 for single tooth indexing error, can be observed on spline teeth having larger indexing error, such as spline tooth #20, #6, #15, #10 and #14. It is also noted when multiple teeth have indexing errors, a sequential engagement behavior will occur. Teeth with larger indexing error have smaller clearance, and they will engage first. Teeth with smaller indexing error have larger clearance and they will gradually come into contact when the torque increases to a certain level [27]. Fig. 18 shows the corresponding loads carried by each tooth of the spline. Tooth #20 has the largest indexing error, therefore the largest ratio of actual tooth load to nominal tooth load would also be observed on tooth #20. Tooth load ratios are 7.0, 5.7, 5.1, and 4.8 at $T = 550$, 1100, 1650 and 2200 Nm, respectively. This indicates that the load concentration resulting from spline tooth indexing error is significant and must be accounted for in the design of a spline at a certain quality level.

## 4. Summary and conclusions

A finite element based computational model of a gear spline-shaft interface under combined torsional load, radial load and tilting moment was proposed. Load distributions of the baseline system of the spline coupling under pure torsion, spur gear loading and helical gear loading were characterized. Pure torsion loading results showed identical load distributions on all spline teeth, with each tooth exhibiting non-uniform load in axial direction. Spur gear loading was shown to cause increased loading on spline teeth whose contact surface normal direction is in the direction of the spur gear meshing force while helical gear loading led to cyclic load concentration oscillating across the face width of the spline teeth.

An extensive parameter study on various variations of the baseline system was performed. Among them, the impact of spline misalignment in relation to spline lead crown was described. Misalignment of the spline was shown to result in a similar load distribution pattern as the case of helical gear loading. Lead crown modifications were shown to significantly reduce load concentrations in misaligned splines. Selecting a helical spline with the same helix direction as that of the helical gear loading the spline could reduce the load concentration and improve load distribution of splines undergoing helical gear loading. Application

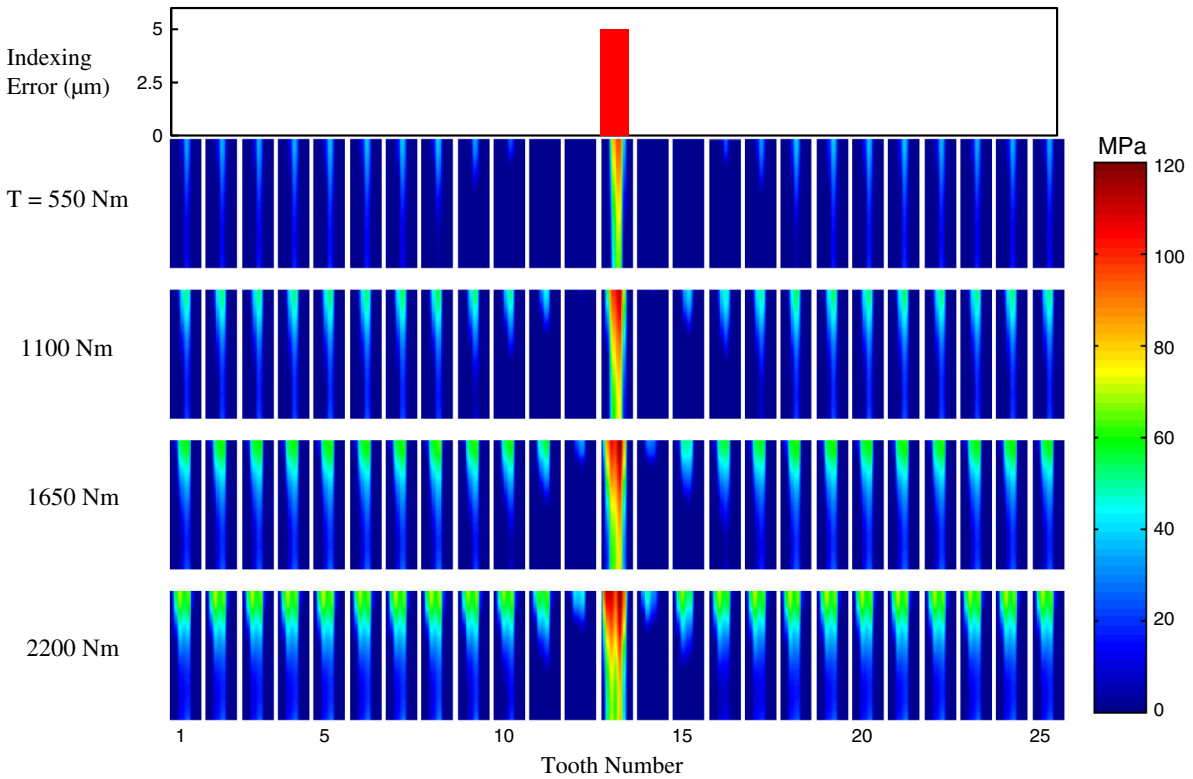


**Fig. 15.** Load distributions of a spline having single tooth indexing error at different torque levels.

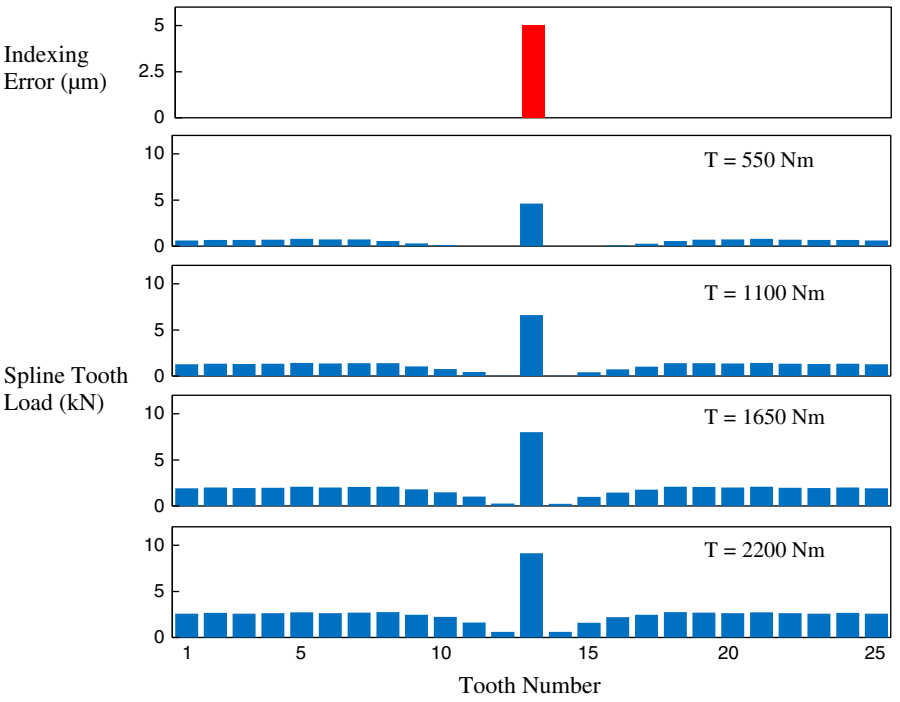


**Fig. 16.** Tooth loads of a spline having single tooth indexing error at different torque levels.

of an optimum intentional lead mismatch to the spline resulted in an even load distribution along the full length of spline teeth by canceling out the torsional "wind up" of the spline shaft. Finally, effects of indexing errors of spline teeth were investigated for the pure torsion loading case to show significant unequal load sharing at spline teeth due to indexing errors.

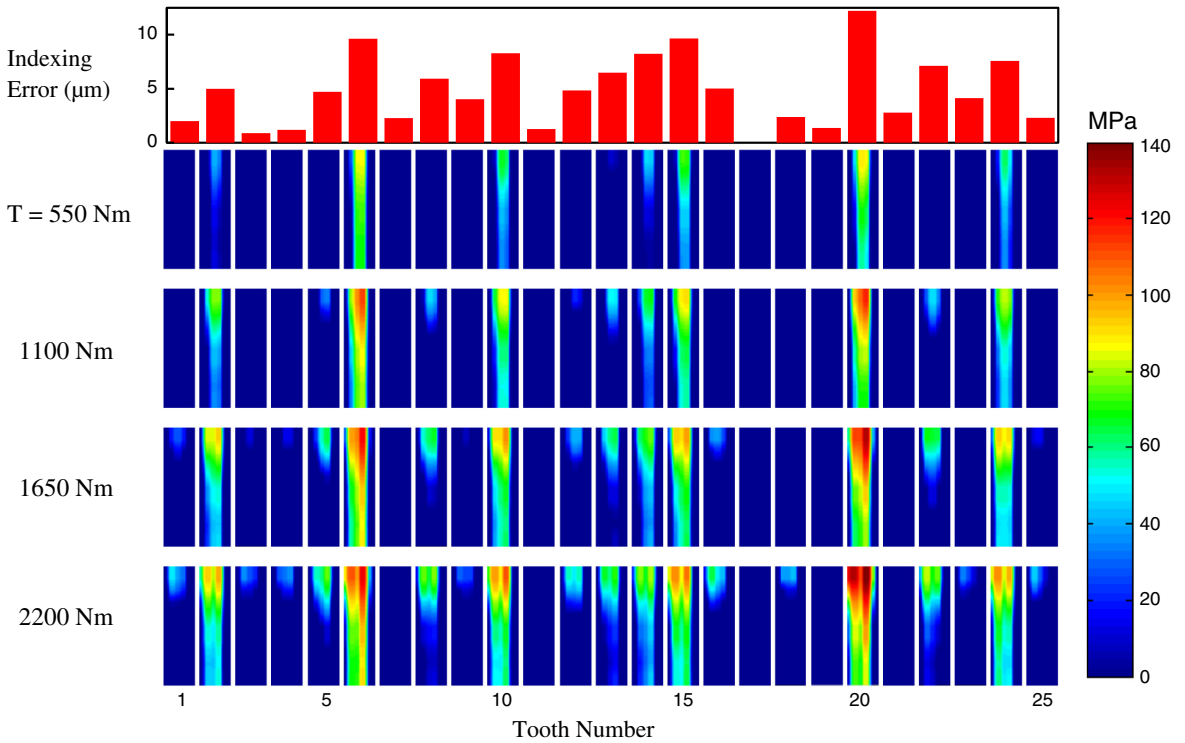


**Fig. 17.** Load distributions of a spline having random tooth indexing error at different torque levels.

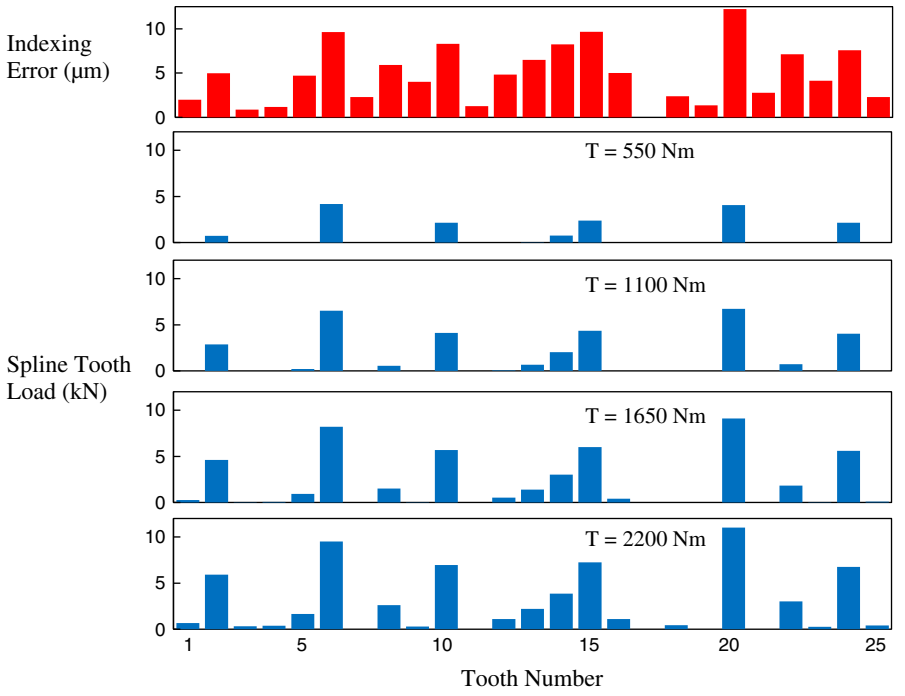


**Fig. 18.** Tooth loads of a spline with random tooth indexing error at different torque levels.

## Acknowledgments

Appreciation is extended to the sponsors of the Gear and Power Transmission Research Laboratory of The Ohio State University whose financial support made this work possible. Authors also thank the Advanced Numerical Solutions, Inc. for making the spline analysis package CALYX available.

## References

[1] P.M. Ku, M.L. Valtierra, Spline wear-effects of design and lubrication, J. Eng. Ind. 97 (4) (1975) 1257–1263.
[2] H.W. Brown, A reliable spline coupling, J. Eng. Ind. 101 (4) (1979) 421–426.
[3] B.P. Volfson, Stress sources and critical stress combinations for splined shaft, J. Mech. Des. 104 (3) (1982) 551–556.
[4] G.K. Tatur, A.G. Vygonnyi, Irregularity of load distribution along a splined coupling, J. Russ. Eng. 49 (1969) 23–27.
[5] A. Barrot, M. Paredes, M. Sartor, Determining both radial pressure distribution and torsional stiffness of involute spline couplings, Proc. IMechE C J. Mech. Eng. Sci. 220 (12) (2006) 1727–1738.
[6] A. Barrot, M. Sartor, M. Paredes, Investigation of torsional teeth stiffness and second moment of area calculations for an analytical model of spline coupling behaviour, Proc. IMechE C J. Mech. Eng. Sci. 222 (6) (2008) 891–902.
[7] A. Barrot, M. Paredes, M. Sartor, Extended equations of load distribution in the axial direction in a spline coupling, 16 (1) (2009) 200–211.
[8] L. Limmer, D. Nowell, D.A. Hills, A combined testing and modelling approach to the prediction of the fretting fatigue performance of splined shafts, Proc. Inst. Mech. Eng. G J. Aerosp. Eng. 215 (2) (2001) 105–112.
[9] Z. Kahn-Jetter, S. Wright, Finite element analysis of an involute spline, J. Mech. Des. 122 (2) (2000) 239–244.
[10] A. Tjernberg, Load distribution in the axial direction in a spline coupling, Eng. Fail. Anal. 8 (6) (2000) 557–570.
[11] A. Tjernberng, Load distribution and pitch errors in a spline coupling, Mater. Des. 22 (4) (2001) 259–266.
[12] S.B. Leen, I.J. Richardson, I.R. McColl, E.J. Williams, T.R. Hyde, Macroscopic fretting variables in a splined coupling under combined torque and axial load, J. Strain Anal. 36 (5) (2001) 481–497.
[13] S.B. Leen, T.H. Hyde, C.H.H. Ratsimba, E.J. Williams, I.R. McColl, An investigation of the fatigue and fretting performance of a representative aero-engine spline coupling, J. Strain Anal. 37 (6) (2002) 565–583.
[14] S.B. Leen, I.R. McColl, C.H.H. Ratsimba, E.J. Williams, Fatigue life prediction for a barrelled spline coupling under torque overload, Proc. Inst. Mech. Eng. G J. Aerosp. Eng. 217 (3) (2003) 123–142.
[15] J. Ding, S.B. Leen, E.J. Williams, P.H. Shipway, Finite element simulation of fretting wear-fatigue interaction in spline couplings, Tribol. Mater. Surf. Interfaces 2 (1) (2008) 10–24.
[16] J. Ding, W.S. Sum, R. Sabesan, S.B. Leen, I.R. McColl, E.J. Williams, Fretting fatigue predictions in a complex coupling, Int. J. Fatigue 29 (2007) 1229–1244.
[17] J. Ding, I.R. McColl, S.B. Leen, The application of fretting wear modelling to a spline coupling, Wear 262 (2007) 1205–1216.
[18] R.A. Adey, J. Baynham, J.W. Taylor, Development of analysis tools for spline couplings, Proc. Inst. Mech. Eng. G J. Aerosp. Eng. 214 (2000) 347–357.
[19] S. Medina, A.V. Olver, Regimes of contact in spline coupling, J. Tribol. 124 (2) (2000) 351–357.
[20] S. Medina, A.V. Olver, An analysis of misaligned spline coupling, Proc. Inst. Mech. Eng. J J. Eng. Tribol. 216 (5) (2002) 269–279.
[21] S. Vijayakar, H. Busby, D. Houser, Finite element analysis of quasi-prismatic bodies using Chebyshev polynomials, Int. J. Numer. Methods Eng. 24 (1987) 1461–1477.
[22] S. Vijayakar, A combined surface integral and finite element solution for a three-dimensional contact problem, Int. J. Numer. Methods Eng. 31 (3) (1991) 525–545.
[23] S. Vijayakar, H. Busby, L. Wilcox, Finite element analysis of three-dimensional conformal contact with friction, Comput. Struct. 33 (1) (1989) 49–62.

[24] S. Vijayakar, H. Busby, D. Houser, Linearization of multibody frictional contact problems, Comput. Struct. 29 (4) (1988) 569–576.
[25] American National Standards Institute, STANDARD ANSI B92.1-1996 Involute Splines and Inspection, Inch Version, 1996.
[26] K.W. Chase, C.D. Sorensen, B.J.K. DeCaires, Variation analysis of tooth engagement and loads in involute splines, IEEE Trans. Autom. Sci. Eng. 7 (4) (2000) 54–62.
[27] A. Kahraman, A spline joint formulation for drive train torsional dynamic models, J. Sound Vib. 241 (2) (2001) 328–336.